Journal of The Electrochemical Society, 2021 **168** 120518

A Model for Investigating Sources of Li-Ion Battery Electrode Heterogeneity: Part II. Active Material Size, Shape, Orientation, and Stiffness

M. Nikpour,[1,*,z] B. A. Mazzeo,[2] and D. R. Wheeler[1,,z]**

[1]*Departments of Chemical Engineering, Brigham Young University, Provo, Utah, United States of America*
[2]*Department of Electrical and Computer Engineering Brigham Young University, Provo, Utah, United States of America*

This work is the extension of our previous paper [Nikpour et al., *J. Electrochem. Soc.* **168,** 060547, (2021)] which introduced the multi-phase smoothed particle (MPSP) model. This model was used to simulate the evolution of the microstructure during the drying and calendering manufacturing processes of four different electrodes. The MPSP model uses particle properties to predict overall film properties such as conductivities and elastic moduli and is validated by multiple experiments. In this work, the model is used to investigate the effects of active material particle size, shape, orientation, and stiffness on graphitic anodes. The model predicts that smaller active particles produce higher calendered film density, electronic conductivity, MacMullin number, and Young's modulus, as compared to larger active particles. Rod-shaped active materials have greater ionic transport and lower electronic transport compared to the disk and sphere shapes, which have similar transport properties. During calendering, disk-shaped particles tend to be oriented horizontally, which decreases through-plane ionic transport. Increasing the stiffness of the active material increases film porosity and composite Young's modulus, while lowering electronic transport and increasing ionic transport.

© 2021 The Author(s). Published on behalf of The Electrochemical Society by IOP Publishing Limited. This is an open access article distributed under the terms of the Creative Commons Attribution 4.0 License (CC BY, http://creativecommons.org/licenses/by/4.0/), which permits unrestricted reuse of the work in any medium, provided the original work is properly cited. [DOI: 10.1149/1945-7111/ac3c1f]

Manuscript submitted July 23, 2021; revised manuscript received November 15, 2021. Published December 10, 2021.

Particle and pore distribution non-uniformities in porous Li-ion battery electrodes can lead to variable internal cell resistances as a result of an uneven arrangement of constituent phases.[1–5] For example, local electronic conductivity can decrease in the areas where more pores exist, or local ionic resistance increases if particles form larger agglomerates that make the ionic pathways more tortuous. Therefore, regional material distribution heterogeneity affects regional ionic and electronic transport properties.

To determine such structure-property relationships, how does one determine the microstructure of an electrode? Experimental electrode reconstruction can be destructive (e.g. SEM/FIB) or non-destructive (e.g. X-ray computed tomography).[6–8] These 3D reconstructions yield significant insight into structures, especially if done at high resolutions (less than 50 nm). The details of the particle arrangement inside the electrode microstructure can be correlated to other experiments on electrode performance such as electronic conductivity, tortuosity, and surface area. However, 3D reconstruction methods can be expensive, time-consuming, and challenging due to the heterogeneous and multiscale electrode structure. An accurate structure model can bridge the knowledge gap and provide detailed information about the microstructure plus the physics that led to a particular particle arrangement.

Multiple mesoscale or microscale structure models for electrode materials have been proposed in the literature. Electrode reconstructions and predictions have used random packing of spherical or ellipsoidal particles,[9,10] random seeding and growth of particles,[11] or a dynamic collision algorithm.[12] Such methods do not necessarily consider physics implicit in different manufacturing procedures. Other models have been dseveloped with the focus on simulating a single lithium-ion-battery manufacturing step.[13–18] A benefit of such structure models is that they can be combined with transport and kinetic models[19–22] to predict cell performance.

A few years ago our group became motivated to develop a particle-based model that, with a single set of parameters, captures the essential physics of multiple sequential manufacturing processes in order to predict the microstructure of a completed electrode. This is similar in spirit to efforts to develop universal force fields in the molecular dynamics simulation community.[23] Two models have been developed that use fundamental forces and interactions to determine particle dynamics and packing during different electrode fabrication steps.[1,18] The multiphase smoothed particle (MPSP) model is the more recent and successful one and is introduced in Part 1 of this series. It is derived from smoothed particle hydrodynamics (SPH) and was carefully parameterized and validated using experimental data.

The model can reproduce and predict different electrode structures resulting from various compositions and active material (AM) types. Based on the predicted structures, one can calculate macroscopic film properties such as conductivities and elastic modulus. To that end, the MPSP model was used to simulate the drying and calendering manufacturing processes for four different electrodes, each with a volume of 30 μm × 30 μm × 80 μm, where the longer dimension is the full film thickness.[1] Films as thick as 150 μm have also been simulated.

The previous model results show the interconnected effect of the manufacturing steps and constituent particle properties on the electrode micrometer-scale variability. For example, calendering can reduce thickness and Young's modulus variations but it does not necessarily eliminate transport-related heterogeneities. According to the proposed multi-phase packing theory, smaller and softer carbon-binder domains (CBDs) tend to accumulate at the top and bottom confining surfaces.

We observed that the distinct anode and cathode active materials led to different conductive and mechanical characteristics of the dried and calendered films. For example, the graphite anode showed higher electronic conductivity and ionic resistance than those of the tested cathodes due to its inherently conductive, non-spherically-shaped, and relatively soft AMs that preferentially align in a specific direction. Between NMC and LCO active materials, LCO leads to higher cathode electronic conductivity and more variable film thicknesses as a result of more diverse AM shapes and sizes. Finally, the small porous HE5050 AM shows the lowest electronic conductivity and ionic resistance.[1]

While the MPSP model was successful in characterizing different types of electrodes, multiple AM particle characteristics were changed at one time and so the unique influence of each characteristic was not finely illuminated. Therefore, this work is designed to better isolate and understand AM particle properties by varying them one at a time. We then assess the effect of particle characteristics on

*Electrochemical Society Student Member.
**Electrochemical Society Member.
[z]E-mail: mojdeh.nickpour@gmail.com; dean_wheeler@byu.edu

Exhibit 2006
Ningde Amperex Technology Ltd.
IPR2023-00587, U.S. Patent No. 10,964,987

microstructure properties. Additional issues with particle orientation are also considered.

The AM size differences among and within AMs (e.g. 2 μm HE5050 vs 2–15 μm graphite) motivate the study for the possible effect of particle size on the electrode microstructure evolution during drying and calendering manufacturing steps. In this work three different size distributions are investigated: uniform large (15 μm), uniform small (4 μm), and poly-dispersed (2–15 μm).

The shape of the active material is another important property. There have been some studies considering new AM shapes[24–27] but there has not been a systematic modeling study of how shape influences the microstructure evolution during manufacturing processes and the subsequent electrode properties that lead to micro-scale heterogeneity. The case studies here are based on three representative AM shapes, namely spheres, disks, and rods.

The rotational asymmetry of irregular (non-spherical) AM can result in anisotropic transport properties of the electrode film. SEM images of graphite anodes show that irregular AM seems to favor a particular orientation during different manufacturing steps (see Fig. 9 below). One can conceive the possibility that during film coating, particle orientations could be controlled. Therefore, this paper will study structural evolution for initially oriented AMs and what effect this has on film properties. Three slurries are simulated with horizontal, vertical, and random AM orientations.

Another noticeable difference among electrodes is the elastic modulus. Stiffer electrodes would be expected to have a higher tolerance to applied pressure but with lower fracture resistance. The AM stiffness can directly affect the electrode response to possible stress sources during manufacturing or cell cycling.[1,28] Two different particle stiffnesses are examined here, roughly corresponding to graphite and a harder form of carbon.

The MPSP model can simulate some aspects of micrometer-scale heterogeneity. One method of assessing the influence of heterogeneity is to repeat simulations with different initial placement of particles. This is indicated by the relative sizes of error bars in the plots below. Another method also used here is to assess the sensitivity of results to a certain particle property (like size).

The remainder of this paper consists of a brief review of the electrode materials and their physical properties, the simulation setup and the experimental design, and a discussion of results for simulated structures for different particle properties.

Electrode materials and their morphological properties

Electrodes are made of different AMs with various compositions, shapes, and sizes (Figs. 1 and 2). $LiCoO_2$ (i.e. LCO) and $Li[Ni_xMn_yCo_{1-x-y}]O_2$ (i.e. NMC) are the most common cathode AMs due to their layered structures that facilitate ion intercalation/deintercalation.[29] These two AMs are typically spherical with rough surfaces due to secondary particles being formed from smaller primary particles (Fig. 2); their secondary particle size varies between 2 and 15 μm. Toda HE5050 is a Li-rich NMC ($Li_{1.2}Ni_{0.15}Mn_{0.55}Co_{0.1}O_2$)[6] that was previously studied in our work due to its significant difference to other cathode materials, namely small porous spherical particles that are approximately 2 μm in diameter.[1] Graphite is the most-widely-used anode AM,[30,31] and is innately electronically conductive. The baseline particles in this work are intended to imitate CPG-A12 graphite particles, which are non-spherical with a size range of 2–15 μm.

In addition to AM, electrodes are composed of additives such as binder and carbon black to enhance the contact between particles. A binder is typically used to bind different electrode materials together and to the current collector. There are water- and organic-based binders with different chemistries and molecular weights. The molecular weight of binder can impact the slurry viscosity and calendered properties. For example, binders with higher molecular weight increase the surface roughness due to higher particle agglomeration.[32] Carbon black particles boost the electronic conductivity of the electrode. In this work, properties of the binder and carbon black are embedded in the model in the form of CBD properties like density, volume fraction, viscosity, and phase conductivity. Density for instance affects how attracted CBD particles are to other CBD particles (cohesion) or to dissimilar particles (adhesion).

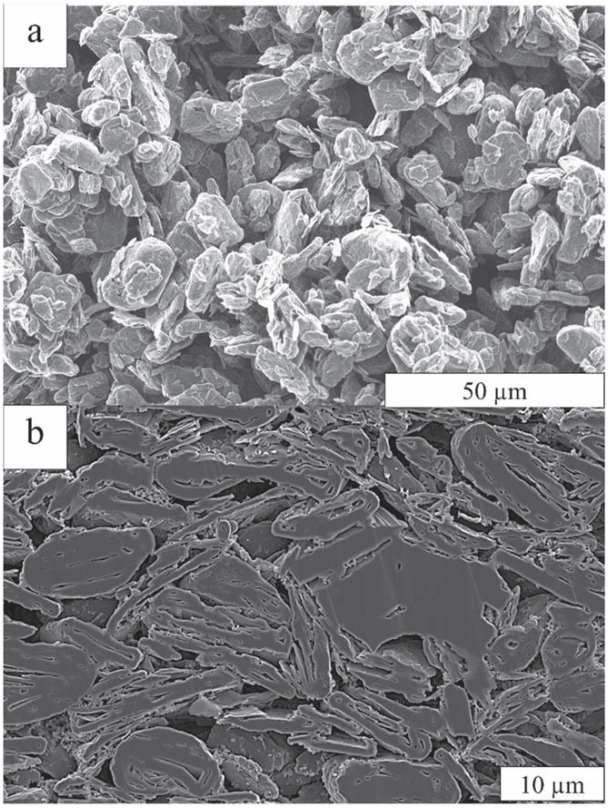


Figure 1. SEM images of various CPG-A12 AM sizes, shapes, and orientations (a) in a top-view of the pure powder, (b) throughout the cross-section of a dried electrode.

Both carbon and binder additives decrease the energy density of the cell due to displacing AM volume in the electrode. The additives can also change the transport properties of the film as they tend to form a nanoporous carbon-binder domain (CBD). Therefore, electrode formulation is an optimization problem involving tradeoffs.[33] The goal is to increase the energy density of an electrode without compromising the mechanical and conductive properties of the cell.

Figure 1 shows the active material properties of the pure AM powder and the dried graphite anode. The significant non-uniform active particle shape, size, and orientation can be observed in this figure. These factors as well as the particle stiffness (which was proven to be an important analyzing tool in part 1) are studied in this paper. The amounts of binder and carbon and the manufacturing processes are kept constant to isolate the effect of these AM characteristics.

Note that the model uses a simplified distribution of particle sizes and shapes, namely one shape (at a time) with up to 7 particle sizes. Furthermore, we compare the more realistic particle size distribution to even simpler cases where there is only one particle size, in order to determine the effect of the size distribution.

Particle size.—The effect of particle size on microstructure impacts many fields and has therefore received considerable attention in prior work. As a general principle, a range of particle sizes leads to smaller particles filling the gaps formed by larger particles. This increases the electrode mass loading (i.e. total mass over an area or volume).[34] Smaller particle size increases agglomerate

Exhibit 2006
Ningde Amperex Technology Ltd.
IPR2023-00587, U.S. Patent No. 10,964,987
Page 2 of 14

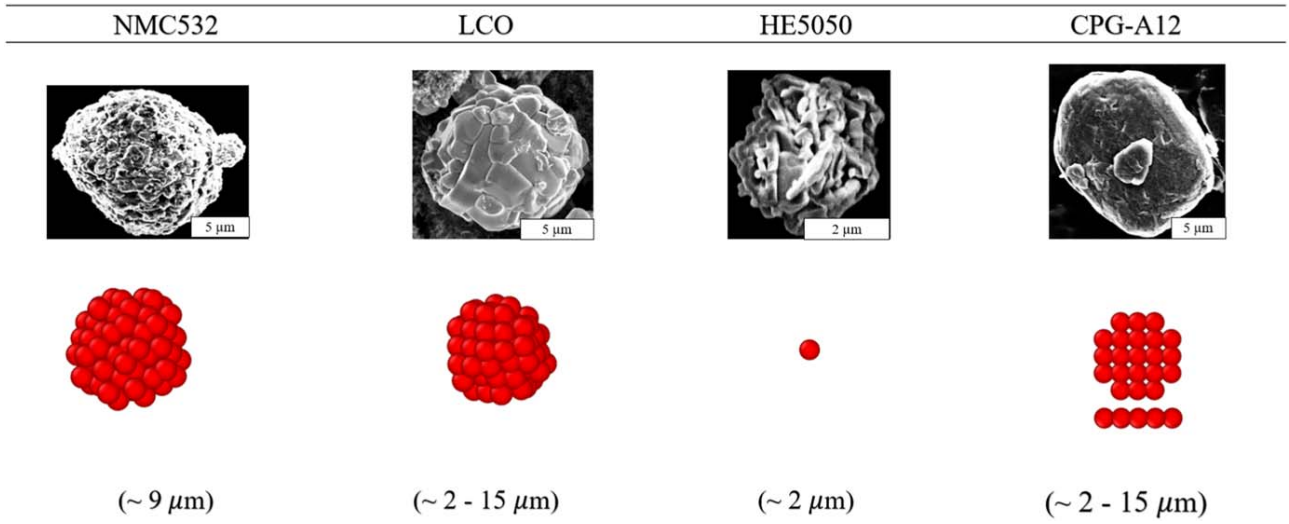


Figure 2. Common cathode and anode active materials with their MPSP model representation (composed of 2 μm spheres) and typical size distributions. CPG-A12 is shown with two different angles to demonstrate the formed disk.

formation.[35] Agglomeration can be understood in terms of attractive forces among particles or the minimization of high-energy exposed surfaces.

A brief summary and analysis of prior work that relates to the four principal electrode manufacturing steps follows.

(1) During mixing, particle size needs to be considered to ensure sufficient mixing. This is due to the effect of particle size on surface energies (particle-to-particle and particle-to-solvent) that can lead to the aforementioned agglomerate formation and non-uniform particle distribution. Generally, smaller particles (AM, carbon, or both) tend to agglomerate more during mixing. Smaller particles also tend to increase the viscosity due to strengthened surface interactions. The goal of mixing is to achieve a homogeneous mixture, which means breaking up the largest agglomerates and thoroughly wetting the components, though the smallest agglomerates are likely less affected.[36]

(2) During coating, viscosity and particle agglomeration continue to be important factors. For instance, the presence of particle agglomerates can lead to an uneven coating thickness.[37,38]

(3) During drying, the size of AM can affect the evolution of the electrode porous structure. For example, the small and soft carbon-binder domain (CBD) phase can redistribute near the current collector after drying based on it filling in the gaps between relatively inefficiently packed and stiffer active material, a phenomenon in Part 1 we termed multiphase packing theory.[1] The size of the particles can also affect the pore network during drying. Previous studies showed that smaller active particles can create a more connected pore structure in the context of soil systems.[27,39] A previous study on $LiFePO_4$ cathode active material showed higher electronic conductivity can result from smaller active material.[40] A comparable outcome is predicted from the MPSP model as shown in the results section below.

(4) During calendering, particle size can affect how the electrode microstructure responds to the applied stress. One effect has been described by multi-phase packing theory: the smaller and softer CBD particles develop higher concentrations at the top and bottom surfaces of the electrode during calendering.[1] Another effect concerns elastic modulus and crack formation. The elastic modulus of the electrode is a function of constituent particles stiffness and particle-to-particle contacts. Smaller AM particles are expected to have more cohesive forces due to higher surface areas and increased contacts, leading to higher elastic modulus.[41] While normally a stiffer material would be more susceptible to crack formation, smaller particles have been found to accommodate initial flaws with less propagation of cracks. This is again due to the higher surface area of the smaller particles that can dissipate more internal stresses.[42]

Poly-dispersity can affect not only the particle arrangement during electrode manufacturing steps but also cell performance during cycling as a result of particle size impact on the effective capacity and Coulombic efficiency.[11,12] Such effects can be explained in terms of diffusion and surface reactions in Li-ion batteries. Generally, smaller AMs have smaller diffusion paths and more exposed surface area to intercalation and solid electrolyte interphase (SEI) formation reactions. Increased area means that the kinetic over potential will be less for smaller particles. This in turn will affect the discharge voltage profile where smaller particles favor faster capacity utilization.[43] According to some previous studies,[43–45] there is an optimal active particle size specific to the AM type to maximize practical capacity. For example, the optimum size is around 0.5–0.8 μm for a thin-layer $LiMn_2O_4$ electrode.[45]

Active material shape.—The shape of the active material is known to affect the porosity and the inter-connectivity of the particles.[27] Previous studies[46,47] show that the shape of the particles affects particle positions and alignments when they are suspended in liquid and experiencing shearing flow.

The effect of particle shape has been studied in the context of percolation theory, which seeks to understand the relationship between volume fractions of conducting and non-conducting phases and the resulting conductive paths.[48] Previous studies by Sastry and coworkers showed that a higher aspect ratio of the conductive additive results in a higher electronic conductivity for the composite. They also found that the contact resistance between the active material and current collector is the lowest for spherical shaped AM and highest for the disk-shaped graphite AM; the rod-shaped AM has an intermediate contact resistance.[49,50]

In this study, we study the effect of AM shape on the transport and mechanical properties of the electrode. Figure 2 shows spherical- and disk-shaped active particles that could represent common cathode and anode materials and that were included in our prior study.[1] Note that the shapes in this work are idealized shapes composed of aggregates of smaller primary particles. In this

Exhibit 2006
Ningde Amperex Technology Ltd.
IPR2023-00587, U.S. Patent No. 10,964,987
Page 3 of 14

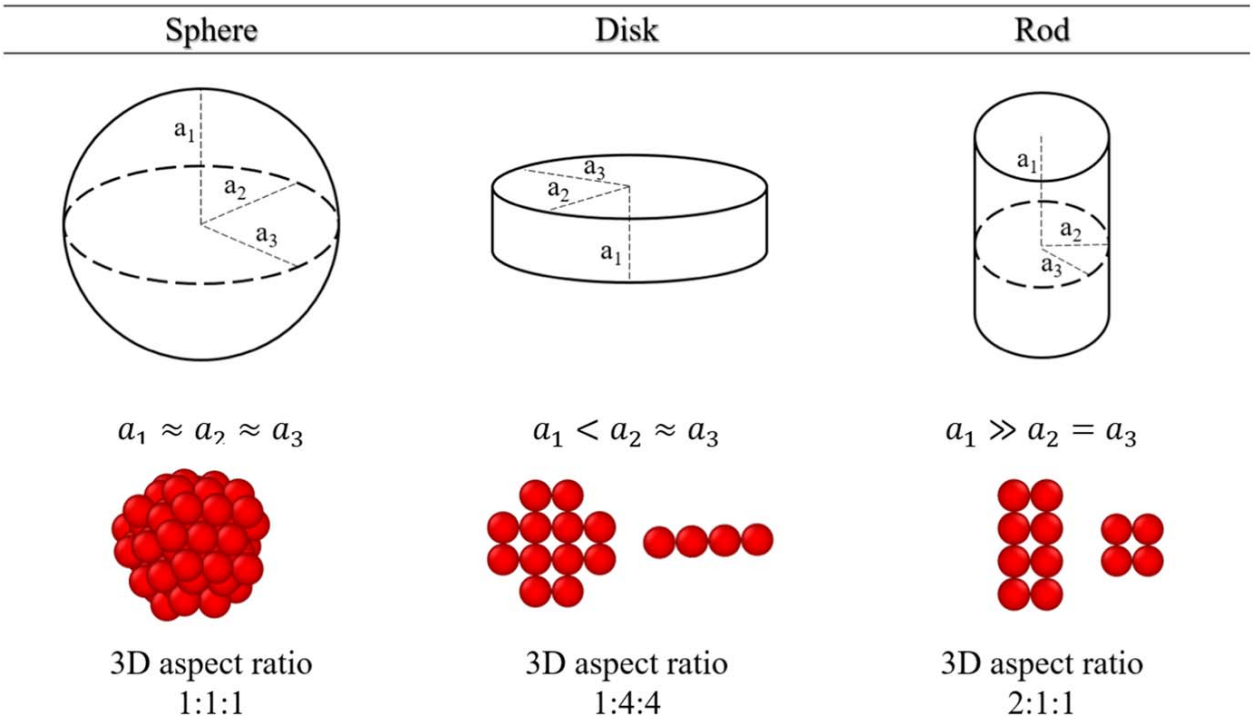


Figure 3. Active particle shapes and their 3D aspect ratio studied in this work.

work, the effect of particle shape is isolated by holding other parameters such as composition, size, orientation, and stiffness constant. Figure 3 shows the different shapes (sphere, disk, and rod), along with their 3D aspect ratios (i.e. height: width: length) that are discussed.

Active material orientation.—The non-sphericity of AM introduces rotational alignment and an increased tendency for anisotropy. Prior work (in the field of drug delivery, not batteries) suggests that a non-spherical particle can reorient according to inter-particle and external forces exerted during a particular mechanical process.[46] Similarly, in electrode fabrication, particle alignment can result from particle-to-particle interactions in which adjacent particles adopt similar alignment in order to minimize free volume or potential energy. External forces also can play a role in aligning particles, such as when an electric or magnetic field[51] is exerted on the film or particles are pressed against a flat surface. Therefore, non-spherical particles can be aligned in nonrandom ways, with particle orientation being a function of the rotational inertia, size, and density of the particles as well as any possible external force. These factors vary from particle to particle for Li-ion battery electrodes, which in turn can contribute to electrode-scale heterogeneities causing non-uniform porosity, particle contacts, and the transport properties of the electrode. Furthermore, studies[1,27,52] have shown that irregular shapes create more anisotropic tortuosity compared to a symmetrical spherical shape. In other words, even though anisotropy in a composite structure is possible with spherical particles, it is made more likely when particles are non-spherical.

Many questions remain on the relationships between particle shape and orientation and resulting electrode performance. In this work, we address one possible question, namely whether controlling the orientation of disk-shaped AM can lead to superior electrode properties. Three initial orientation schemes are studied (Fig. 4). The angle distributions of the disk-shaped AMs are analyzed at each step to determine the degree of particle rearrangements during the drying and calendering processes and how these affect transport and mechanical properties.

Active material stiffness.—Particle stiffness controls the electrode response to possible stress sources during electrode fabrication or cell cycling. Electrode manufacturing (the focus of this work) involves multiple stress sources especially during calendering that can alter the structure. Stiffer particles exhibit lower plastic deformation and a higher tendency to fracture under possible stresses. Fractures can lead to particle separation affecting the transport properties of the electrode. Our previous study indicated a meaningful difference among the mechanical stabilities of the examined electrodes. Such difference motivates more investigation into the effect of AM stiffness on the dried and calendered microstructures.

Each electrode component has a different stiffness value which can lead to stiffness heterogeneity: (1) carbon black is a relatively stiff particle ($E = 80$ GPa[53]), (2) polymeric binder is a soft component ($E = 40$ MPa[54]), and (3) active material can be stiff in the case of metal oxide cathodes ($E = 175$ GPa)[55] or soft in the case of graphite anodes ($E = 16$ GPa).[56]

Simulation and Experimental Procedures

MPSP model.—The multi-phase smoothed particle (MPSP) model for predicting 3D electrode microstructure is implemented in LAMMPS (Large-scale Atomic/Molecular Massively Parallel Simulator) software.[57] The development, parameterization, and application of the model are discussed previously.[1] The simulation source code, input files, and example structures are archived on GitHub.[58]

Table I gives the particle properties for the simulations here, based on the CPG-A12 anode used in the previous study. The simulated dry weight composition is 92% CPG-A12 active material, 6% polyvinylidene fluoride (PVDF), and 2% carbon black. N-methyl-2-pyrrolidone (NMP) is used as the solvent. Anodes made by an aqueous process obviously have different binder and solvent, but the coarse-grained nature of this model (e.g. CBD particles are described in terms of properties in Table I) means it also could be applicable to such systems. The baseline AM case is less stiff, and a stiffer variant AM is given as well. AM particle stiffness is

Exhibit 2006
Ningde Amperex Technology Ltd.
IPR2023-00587, U.S. Patent No. 10,964,987

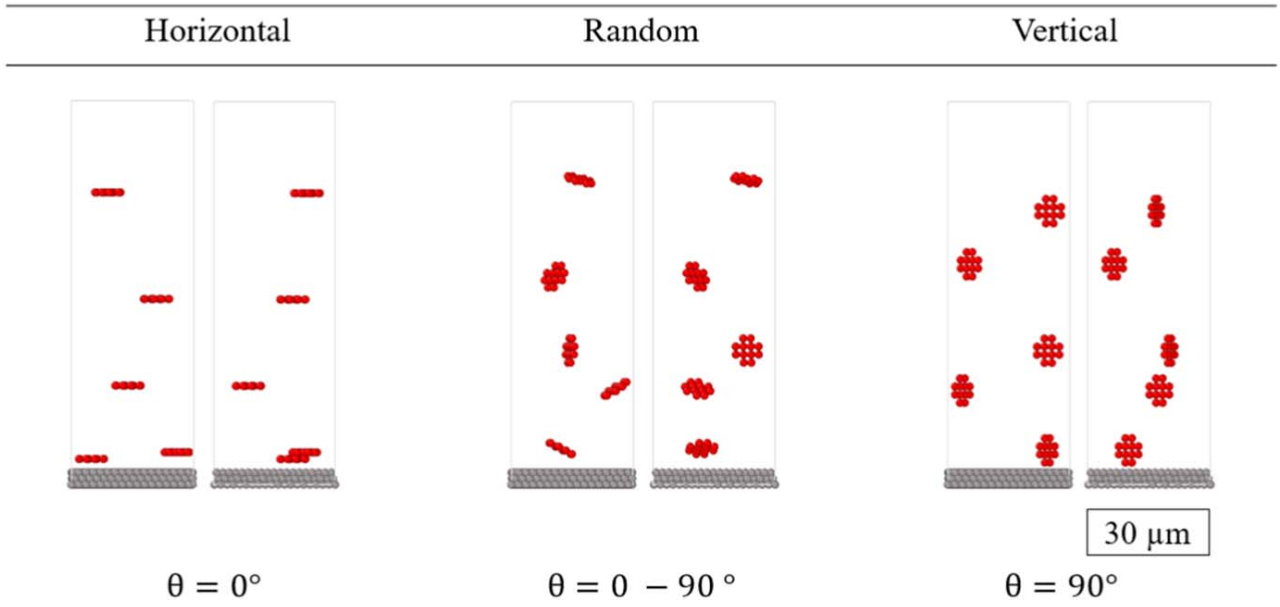


Figure 4. Illustration of different orientations of the AM. Note that in the actual simulation there are many more active particles along with solvent and CBD particles present in the slurry.

Table I. MPSP model interaction parameters.

Parameter		CBD	Solvent	Active baseline	Active stiff
Smoothing length	h (μm)	2.2	3.0	2.7	2.5
Speed of Sound	c_0 (m s^{-1})	150	3	200	500
Viscosity	μ (mPa.s)	61.4	1.6	61.4	61.4
Rest density	ρ_0 (g cm^{-3})	2.5	2.5	2.3	2.2

controlled through particle parameters of smoothing length, rest density, and speed of sound as previously discussed.[1]

Drying and calendering simulations.—The drying and calendering simulations are intended to mimic the actual processes. A "network-favored" drying scheme is used for drying in which solvent particles are sequentially deleted to represent the evaporation of the solvent. Preferential deletion happens for particles closer to the upper surface or that are part of larger aggregates or reservoirs of liquid particles. In other words, liquid in larger and more accessible pores evaporates first, and eventually all liquid particles are deleted. One important consideration is due to the timescale difference between simulated and experimental drying that the simulated drying is more conceptual. Specifically, solvent particles are deleted in a particular sequence that imitates but doesn't precisely correspond to a certain experimental drying rate or temperature.

The calendering procedure involves a constant-speed compression until the film thickness reaches 39 μm resulting in a porosity around 30%–35%. The wall is held stationary to allow the structure to equilibrate and then is raised.

The MPSP model used here does not consider cracking internal to the AM particles; though we recognize that this is an important phenomenon for describing the mechanical response to calendering in some cases, and more importantly to lithium intercalation. Such cracking does depend of course on the size, shape, and stiffness of the AM and will affect cell performance.[59,60]

Post-simulation analysis.—Mechanical and transport properties can be derived from the structures resulting from the drying and calendering simulations.

Young's modulus.—The Young's modulus before and after calendering is determined from the initial and final slopes of the stress-strain curve during the compressive calendering process.

Segmentation.—In preparation for conductivity and surface area calculations, the particle-based microstructure is mapped onto a grid of cubic voxels of size 0.4 μm. A single representative constituent phase is assigned to each voxel: active, low-density CBD, high-density CBD, or micropore. The reason for the two different CBD types is to better account for the effect of compression on CBD electronic and ionic properties. To do the differentiation, the interpolated SPH particle density of each phase is calculated at the center of each voxel. A voxel is assigned as active if the active phase density is between 1.3–1.9 g cm^{-3}. The active phase density cut-offs are set for each electrode to conserve the mass fractions of AM and CBD before and after calendering. If that condition is not met, the voxel is assigned as a high-density (HD) CBD voxel if the CBD density is higher than 1.1 g cm^{-3}, else it is assigned as low-density (LD) CBD if the density is higher than 0.1 g cm^{-3}. If none of these conditions are met, that voxel is assigned as a pore.

Simulation values of porosity are calculated based on the segmented structure. This overall porosity accounts for the porosity contributed by the pore voxels as well as the nanoporosity contributed by the CBD voxels (55% and 35% porosity for LD and HD respectively). This method of calculating porosity is different than the experimental approach of measuring the film thickness and mass.

Conductivity calculations.—Effective ionic and electronic conductivities of the entire film are then determined by finite volume

Exhibit 2006
Ningde Amperex Technology Ltd.
IPR2023-00587, U.S. Patent No. 10,964,987
Page 5 of 14

Table II. Assigned domain conductivities for segmented voxels. Values indistinguishable from zero are so-indicated.

Conductivity type	CBD		Pore	Active
	Low density	High density		
Electronic (S cm^{-1})	1.5	2.7	~0	11.0
Ionic (S cm^{-1})	0.0025	0.001	0.01	~0

calculations.[22] An electric potential difference is imposed across the segmented structure, and the local potential distribution is calculated from local conservation of current and the conductivity assigned to each voxel. The total current through the structure then determines the effective film conductivity. The domain conductivities given in Table II are based on prior experiments.[1]

Surface area.—The surface area between AM and the CBD and pore phases is an indicator of electrochemical accessibility of the AM and also an indicator of the degree of aggregation. Surface areas are calculated from the identities of adjacent voxels in the segmented structure, meaning if two adjacent voxels are of dissimilar phases then this is accumulated as interfacial area. It is normalized by the mass of AM. This calculated surface area does not reflect nanoscale roughness but can provide additional information on particle-to-particle arrangement among different conditions investigated in this study. For instance, if this coarse-grained surface area is reduced, this suggests a larger degree of agglomeration of the active material.[39]

AM angle.—The angle between the short axis (a_1) of disk-shaped AM and the through-plane direction indicates orientation. For the vertical alignment case, this angle is uniformly 90 degrees before drying commences and for the horizontal case, the angle is initially zero. The random case is based on a random angle selection between 0 and 90 degrees. These distributions at the conclusion of the drying and calendering simulations are re-evaluated.

Electrode preparation and cross-section.—To produce the images in Fig. 9, the procedure was as follows. Phillips 66 CPG-A12 AM (92 wt%) and TIMCAL carbon black (2 wt%) were dry-mixed by mortar and pestle for 20 min with an intention to break up any aggregates without fracturing particles and disperse the carbon black evenly among the AM. NMP solvent and Kureha 9300 PVDF binder (6 wt% after drying) were mixed separately for 30 min to activate the binder and to create a uniformly dispersed mixture. All the components were then wet-mixed for 20 min with an immersion blender (8400 rpm) in an ice bath to prevent heating of the slurry and accompanying evaporation of NMP. The electrodes were coated on a metal foil using a doctor blade. The drying process was carried out under an IR lamp for 10 min. A thermocouple located on the current-collector measured a starting temperature around 150 °C and a temperature around 200 °C at the end of drying. The film was calendered between two metal rollers until a porosity of 30%–35% was achieved. For the pre-dried result in Fig. 9, a separate wet coating was freeze-dried at a temperature of −27 °C under a cold gas stream.

The electrode films were milled using a broad ion beam (IB-19530CP JEOL cross-section polisher) for 2 h at an ion beam voltage of 5 kV. A FEI Helios Nanolab 600 scanning electrode microscope (SEM) was used to study the electrode microstructure. is

Results and Discussion

In this section, the MPSP model is used to make predictions about how various factors create heterogeneity and to explore the parameter space for electrode design. The microstructure properties are assessed in terms of film thickness, porosity, AM surface area, electronic conductivities in the through-plane direction, MacMullin number (ionic resistance) in the through-plane direction, and Young's modulus.

Active material size.—Figure 5 shows the cross-sections of simulated microstructures after coating, drying, and calendering for large, mixed, and small disk-shaped active material, plus the physical and transport properties of the dried and calendered films (e.g. film thickness, porosity, AM surface area, electronic conductivity, MacMullin number, and Young's modulus).

The model predicts the effect of active material size on dried electrode properties. After drying, large AMs function as a structural backbone which can cause higher film thickness and a slightly more porous microstructure (Figs. 5d and 5e). However, the dried MacMullin numbers are similar for all cases suggesting that although the larger case created a slightly more porous structure, the pores are not as interconnected (Fig. 5h). Based on film thicknesses, small AMs with a higher surface area per volume can cause higher film shrinkage and greater AM agglomeration. Therefore, smaller particles provide more electronic pathways as they form active-active agglomerates. Such more-frequent contacts among small particles were reported by another numerical study.[61] Despite the lower overall porosity, the pore network is still more interconnected for the small-particle case. The mixed case electronic conductivity (Fig. 5g) is between the other two cases where smaller particles fill the gaps among larger ones creating a higher degree of interconnections compared to the large case. Smaller particles show a higher elastic modulus (Fig. 5i) after drying and calendering, in agreement with our previous paper.[1] A study by Pang et al. on structures of polydisperse coal particles[41] relatedly notes that loose particles, or particles that are not part of the structural backbone, can result in a lower Young's modulus for the mixture.

Calendering has a different effect depending on the particle size distribution. As shown in Fig. 5, the porosity decreases more (26% change) for mixed and small cases compared to the large case (22% change) after calendering. For the smaller particles, calendering pressure leads to further active agglomerate formation as reflected in the surface area decrease, whereas the surface areas for the large and mixed cases remain rather constant. In general, the transport properties of the small and mixed cases are similar after calendering. Between the large and small AM cases, the higher electronic conductivity of the small-sized AM is a reflection of its state of aggregation. Furthermore, the ionic resistance of the large case is lower due to the interconnected pore network.

The results in this section indicate the potential of designing a gradient-type electrode with smaller particles near the current collector (to have higher contacts between the active particles) and larger ones near the separator (to facilitate ion transport). Such a design also could improve utilization of active material across the thickness of the film at higher charge and discharge rates.[43]

Active material shape.—Figure 6 shows the effect of AM shapes (randomly oriented disk, sphere, and randomly oriented rod) on electrode properties.

The electrode thickness and porosity after drying provide information on how efficiently particles can pack. Shrinkage ratio or relative change in thickness was highest for disk-shaped AM (29% vs 24% for sphere and 11% rod). The electrode with rod-shaped particles shrinks less after drying due to the lack of efficient particle packing, i.e. a more open structure for the electrode. Previous studies have shown that rod-shaped particles have lower packing density compared to spherical shapes when packed randomly.[62,63] This means that rods have fewer contacts and they are randomly distributed. Prior work has suggested that randomly arranged spheres will pack more efficiently than randomly arranged disks; a similar effect is observed in the drying process here, in terms of the void ratio or porosity.[64,65]

Normally one would expect dried film thickness and porosity to be proportional for a given composition. In this work, that

Exhibit 2006
Ningde Amperex Technology Ltd.
IPR2023-00587, U.S. Patent No. 10,964,987
Page 6 of 14

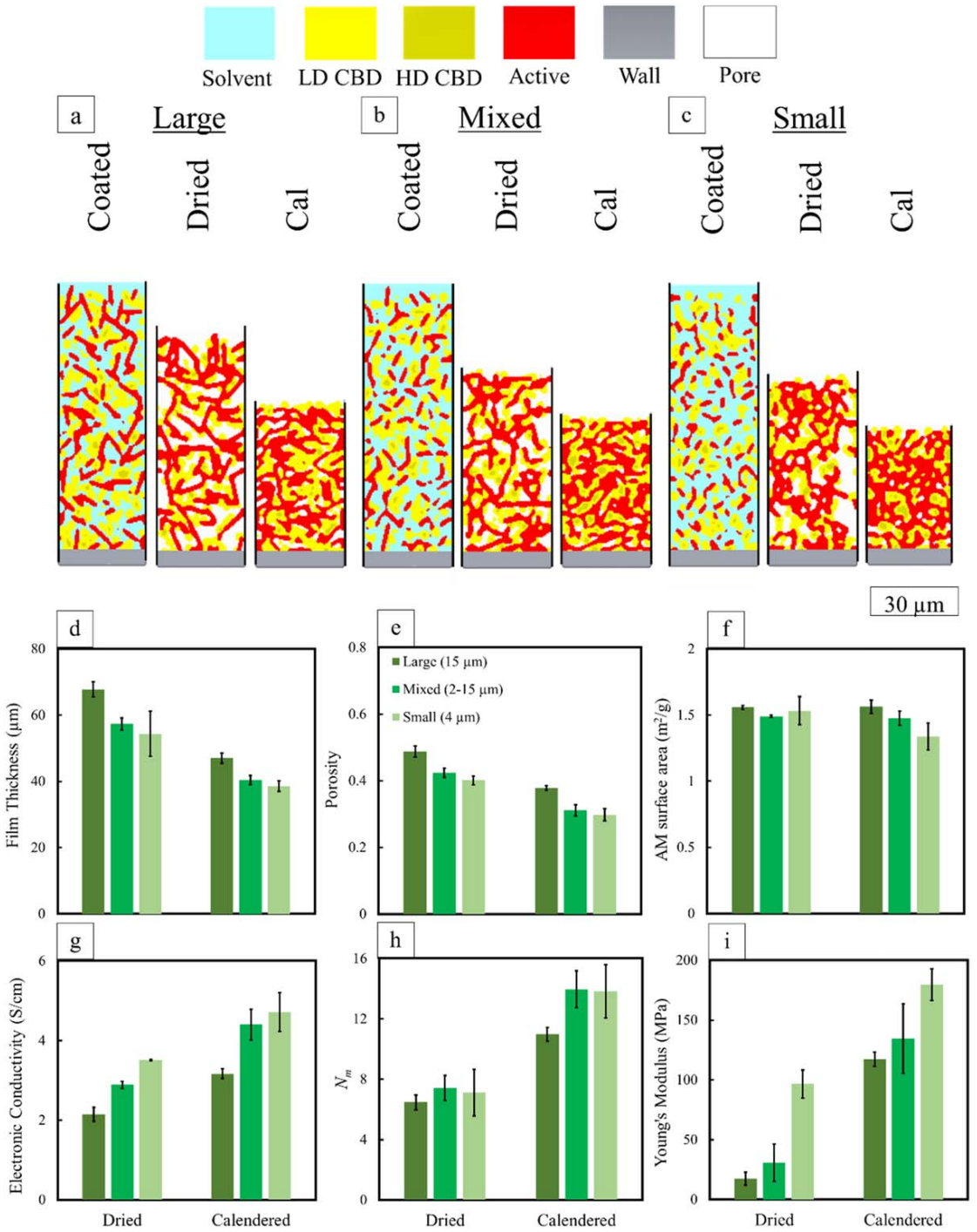


Figure 5. Simulated cross sections for (a) large, (b) mixed, and (c) small sizes of disk-shaped AM at three stages of coated, dried, and calendered (cal). LD and HD denote high- and low-density CBDs. The simulated dried and calendered (d) film thickness, (e) porosity, (f) AM surface area, (g) electronic conductivity, (h) MacMullin number, and (i) Young's modulus.

connection is maintained for all cases except for disk vs sphere in Fig. 6. The discrepancy is due to the way that overall porosity is estimated, namely by combining the volume of large pores plus a portion of the volumes of the low- and high-density CBD (i.e. due to nanoporosity). Here the disk case has a higher fraction of high-density CBD, with lower nanoporosity, compared to the sphere case.

As-dried results show an interesting difference between the conventional cathode and anode AM. Typically Li-ion cathode materials are spherical and graphite anode materials are more irregular. After drying, the spherical AM particles show higher electronic conductivity associated with higher particle-to-particle connection compared to disk-shaped AM. Relatedly, we observe (Fig. 6b) that there is a coating of CBD around the sphere-based clusters in contrast to the other cases where CBD form its own clusters. These results indicate that despite the higher electronic conductivity of the graphite anode (because of its intrinsically

Exhibit 2006
Ningde Amperex Technology Ltd.
IPR2023-00587, U.S. Patent No. 10,964,987

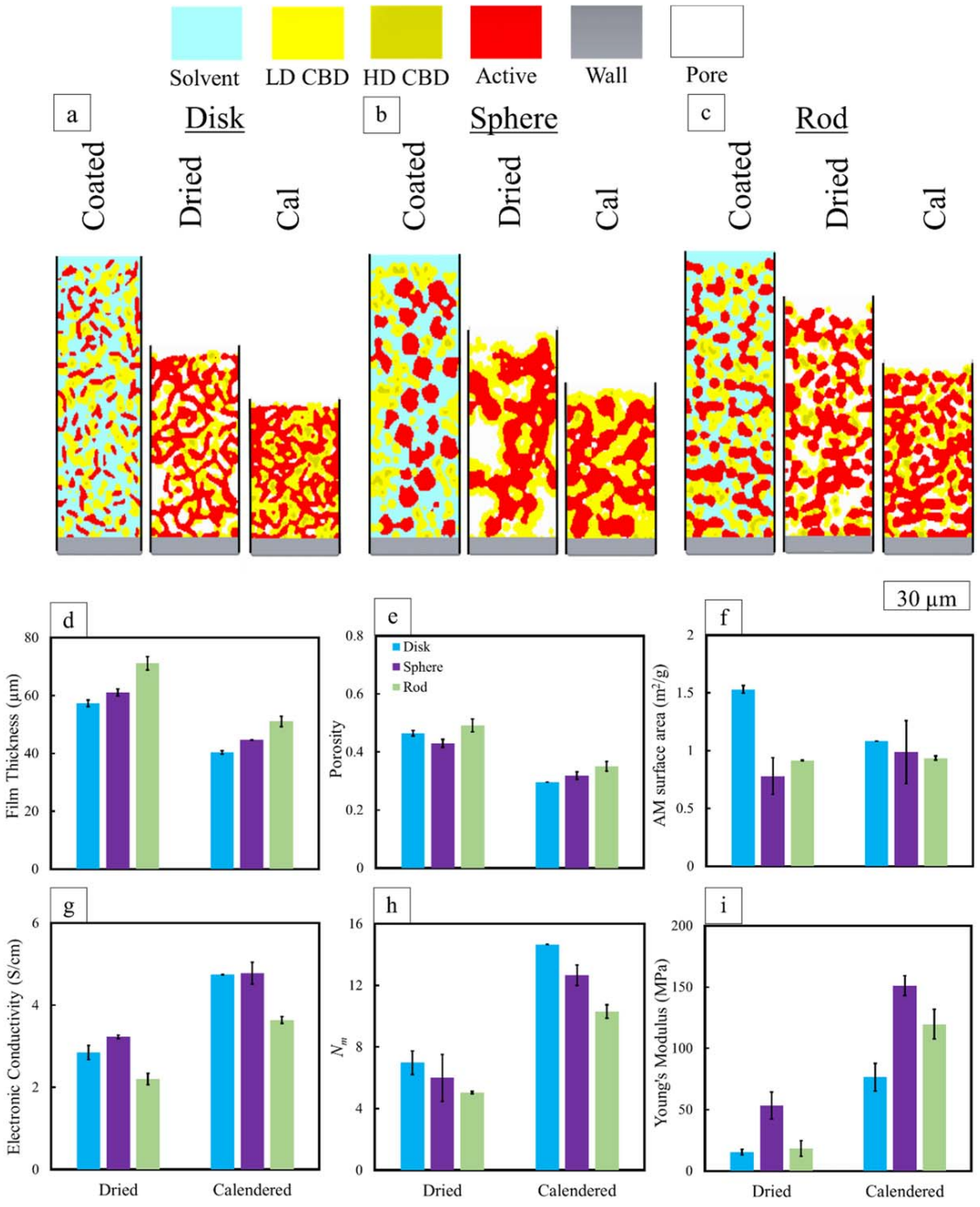


Figure 6. Simulated cross sections for (a) disk, (b) sphere, and (c) rod AM shapes. Remainder of the properties (d)–(i) are the same as those in Fig. 5.

conductive AM), the typical spherical shape of the cathode AM has the potential to provide more pathways for the electrons. The rod-shaped AM shows the lowest electronic conductivity and MacMullin number as a result of its lower packing density that leads to distinctive higher porosity after drying.

The elastic modulus of these shapes shows an interesting trend in agreement with the study by Cho et al.[65] Particle irregularity (non-sphericity) results in a decrease in stiffness. This can be explained by particle rotation and contact slippage for disk and rod shapes that can consume the shear stress. Also, AM irregularity boosts looser packing and therefore a softer network.[65]

Calendering has differing effects depending on the active material shape. The primary effect driving electronic conductivity of a composite is the volume fractions of the phases. In the case of rod-shaped active material, its higher porosity means a lower volume fraction of conductive solids and therefore a lower electronic conductivity. Similarly, ionic resistance (MacMullin number) is lower in this case. In all cases, the increased electronic conductivity and ionic resistance after calendering are mostly due to the compression of micropores and nanopores inside the CBD phase.

The relative amounts of low-density and high-density CBD phases change with active material shape and during the calendering

Exhibit 2006
Ningde Amperex Technology Ltd.
IPR2023-00587, U.S. Patent No. 10,964,987

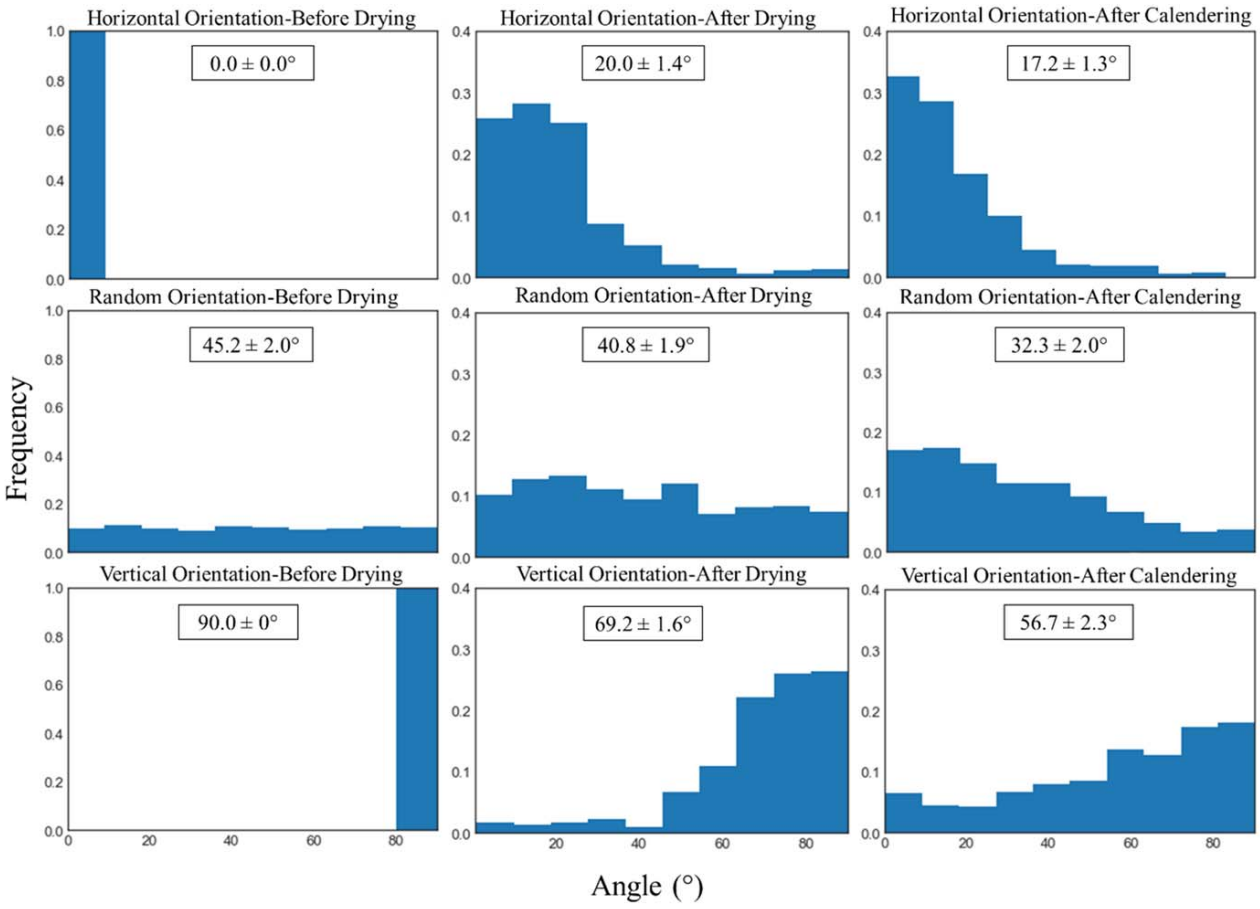


Figure 7. Angle histograms of the disk-shaped AM at the initial (pre-dried), dried, and calendered stages. The vertical axis is frequency or probability, arbitrarily scaled. The angle is between the rotational axis of the disk and the film normal axis. The average particle angle and 95% confidence interval are given in the insets.

step. The volume fractions of the more-conductive high-density (HD) CBD are 2% and 4% for the disk shape, before and after calendering respectively. For the sphere these fractions are 0% and 1%; for the rod shape they are 3% and 3%. These results suggest that calendering compresses the CBD to greater degree for the disk shape. This can explain why the disk-based electrode, which had a lower electronic conductivity before calendering then matches the sphere-based electrode after calendering. For the sphere the majority of the CBD is in the low-density form. As for the rod shape, its electronic conductivity compared to the sphere shape is a relatively constant ratio before and after calendering.

In addition to volume fractions, conductivity of composites is affected by the connectivity or morphology of the most conductive phases, which for electronic conductivity is the active material in this study. One way to assess the connectivity of the active material is by its surface area; lower surface area means more connections or agglomeration within the active phase and higher surface area means less agglomeration and more connections to pores and CBD. In Fig. 6 the most significant point is the relatively high surface area of the disk shape before calendering and the relatively equal amount of surface area for all shapes after calendering. This further explains why the disk-based electrode "catches up" to the sphere-based electrode after calendering, with respect to electronic conductivity. Such a high level of rearrangement for disk shapes upon calendering is in agreement with the experimental study conducted by Dreger et al.[66] On the other hand for spherical AM, the calendering pressure acts as a deagglomeration driving force, due to a modest increase in surface area, though the change is not statistically significant.

The disk-based electrode has the highest ionic resistance after calendering even though the value was similar to the other electrodes before calendering. This appears to be caused by the tortuous pathways generated by the disk shape that is further explored below with respect to particle orientation.

During calendering all three electrodes exhibited plastic compressive strain in the range 27%–30%. Even though the calendering process attempted to compress each electrode to the same thickness, subsequent relaxation of the microstructure meant that the rod-shaped AM maintained the highest porosity after calendering, and this appears to drive the observed ionic and electronic transport differences from the other electrodes.

Active material alignment.—Figure 7 presents the angle histograms and averages (over the whole population for one of the three trials) of the disk-shaped AM at the initial, dried, and calendered stages. The model predicts that drying and calendering make the angles more uniformly distributed and isotropic. Furthermore, calendering produces a notable reorientation toward zero angle (disks lying flat). Nevertheless, particles tend to stay near their initial orientation through both manufacturing processes. Increased variation in angle (less peaked distribution) can cause some variations in electrode properties as detailed in Fig. 8.

Figure 8g shows that after drying the through-plane electronic conductivities of the dried electrodes vary only slightly for different particle alignment schemes. Initial vertical alignment creates the highest through-plane electronic conductivity due to fewer needed interparticle connections along the vertical path.

Exhibit 2006
Ningde Amperex Technology Ltd.
IPR2023-00587, U.S. Patent No. 10,964,987
Page 9 of 14

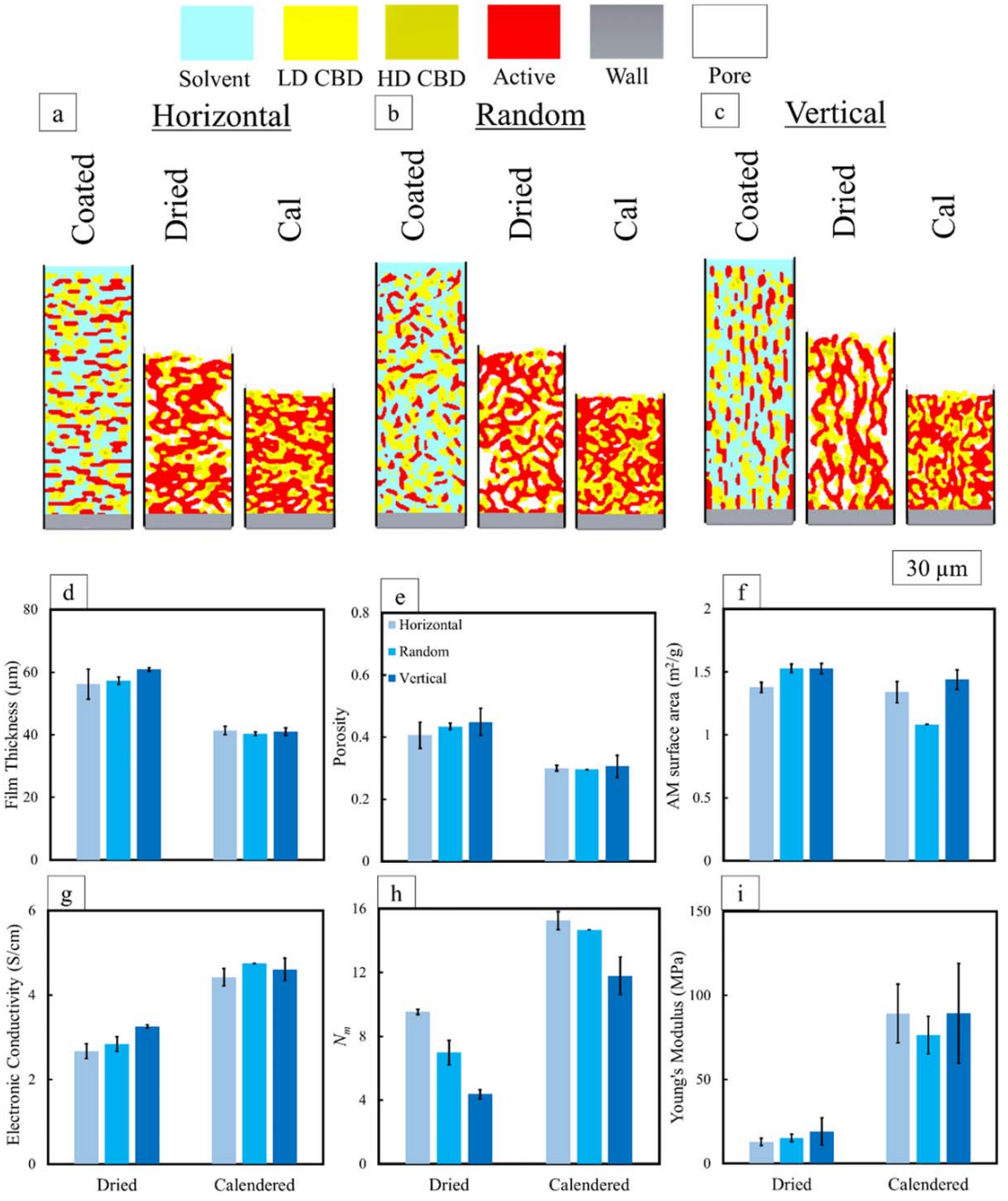


Figure 8. Simulated cross sections for (a) horizontal, (b) random, and (c) vertical orientations of disk-shaped AM. Remainder of properties (d)–(i) are the same as those in Fig. 5.

As for ionic resistivity (N_m in Fig. 8h), a more significant difference is observed, with the vertical orientation producing a less tortuous path as expected. The lower AM surface area (i.e. the exposed surface area to CBD and pore phases) for the horizontal case implies high connectivity between active particles, which can make the tortuosity higher. The random-orientation electrode is the combination of the horizontal and vertical cases and therefore its ionic transport behavior falls between the limiting cases. The relative effect of initial particle orientation is less pronounced after calendering for both ionic and electronic pathways. In other words, calendering tends to reduce the effect of initial differences.

It would be generally expected that ionic and electronic transport would be inversely correlated, meaning that any change that would increase one would decrease the other and this is observed here. However, in this instance, ionic resistances are more sensitive to changes in orientation than are electronic resistances.

The slightly higher Young's modulus of the vertically-oriented dried electrode is expected from standard mechanical analysis in the field of composites (typically in the context of fiber composites), meaning that maximum resistance to deformation is found in the direction of the longest particle length.[67]

The model has the capability to predict the orientation evolution during drying and calendering steps. It is natural to attempt to validate the model results. To the best of the authors' knowledge, the transport and mechanical properties for different active material orientations have not been studied for Li-ion electrodes, so there are

Exhibit 2006
Ningde Amperex Technology Ltd.
IPR2023-00587, U.S. Patent No. 10,964,987

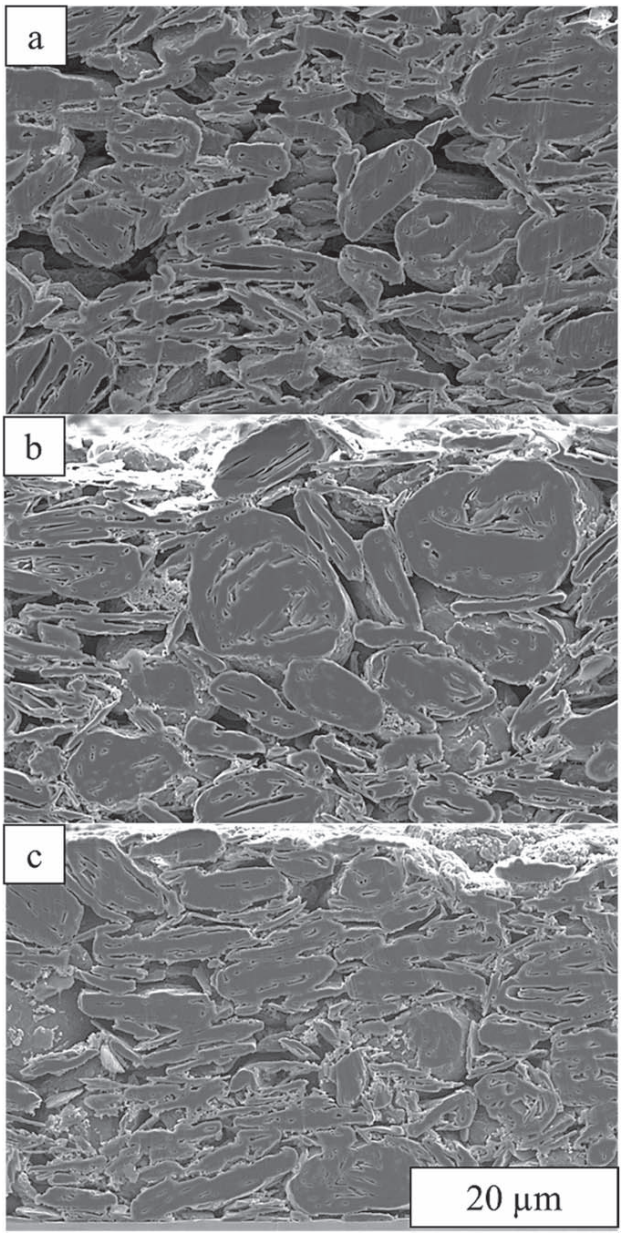


Figure 9. SEM image of a graphite anode at 3 stages of manufacturing: (a) pre-dried, (b) dried, (c) calendered.

few experimental results to validate the predictions made here. We have made 2D cross-sections of graphite electrodes in order to obtain some qualitative information on microstructures. Nevertheless, it is important to recognize that such images do not have adequate information content to perform a full structure comparison between the simulation and experiment.

Figure 9 gives representative SEM cross-sections of a graphite anode after coating, drying, and calendering, and qualitative differences are observed. Figure 9a shows the microstructure of the anode after coating, obtained by freeze-drying the wet sample. Many particles are horizontally aligned although some level of randomness is also observed in the structure. Such horizontal alignment could be due to the shear stress applied by the doctor blade during the coating process. This is in agreement with previous studies that observed the tendency of elongated particles to align to the flow streamlines.[46,52] After drying (Fig. 9b), particles still align horizontally, though with increasing orientation randomness toward the top surface of the electrode. However, after calendering, more particles appear to align horizontally due to the vertical compression. To better tie these SEM images to the model results quantitatively, Figs. 9b and 9c were segmented to get the porosity of the films. The porosity values of the dried and calendered structures are 0.42 and 0.30 respectively which is close to the porosity values of the horizontal case in Fig. 8 (0.43 and 0.30 respectively). We also tried to relate the directional properties of the 2D cross-sectional images (Figs. 8 and 9) to the frequency spectrum in the 2D Fourier domain.[68] However, we found the experimental images (Fig. 9) did not contain sufficient information to exceed noise levels to make quantitative conclusions. Thus, these experimental results can only qualitatively confirm the model predictions, which indicate that an initial horizontal orientation of particles can slightly change during different manufacturing steps. Therefore, if preferred orientations could be maintained, then modest improvements to electrode performance are possible.

Active material stiffness..—Figure 10 shows the physical and transport film properties for two disk-shaped AMs with different rigidities. The stiff case was given a Young's modulus higher than typical for graphite and more characteristic of cathode materials. (Specifically, the higher modulus matches that for the HE5050 cathode in our previous study.[1])

After drying, the stiff particles do not agglomerate as much as for the soft case. This is shown by the higher film thickness, porosity, and exposed surface area of the AM in contact with CBD and pore phases. The stiff case leads to lower ionic resistance as lithium ions can travel through the more connected pores between the particles. The stiff case likewise reduces the electronic conductivity due to poorer contact between active particles. Finally, the higher Young's modulus of the dried electrode is the result of stiffer active particles even though it is a less-dense structure.

Calendering does not diminish the property differences between the soft and stiff cases in general. However, calendering affects the relative ionic transport in the soft case more dramatically: calendering increases the MacMullin number by factors of 2.1 and 1.2 for soft and stiff cases respectively.

Conclusions

The prediction capability of the model is used here to investigate the effect of different AM properties (i.e. size, shape, orientation, and stiffness) on electrode thickness, porosity, conductivities, and Young's modulus. The effect of AM properties on microstructure features of anode-like materials may be summarized as:

(1) The AM size distribution had little effect on MacMullin number of dried electrodes, though there was a slight noted reduction in ionic resistance for the large-particle case after calendering.
(2) Although one would expect smaller particles to have more surface area, in practice the greater degree of aggregation means that exposed or electrochemically active area is not necessarily higher when compared to larger particles.
(3) As expected, smaller AMs create better contacts among active particles that can boost electronic conductivity compared to larger particles. In the case of variable AM sizes, smaller particles will fit into gaps between larger particles giving the mixed-size case higher electronic conductivity than for the large-particle case.
(4) The shape of the AM affects the packing density of the electrode that subsequently alters the transport properties of the electrode. Spheres tend to provide more electronic pathways before calendering due to higher packing density.
(5) The orientation of an irregular disk-shaped AM appears to have little effect on electronic transport and a more significant effect on ionic transport. Note that these results are based on initial orientations prior to the drying process, during which

Exhibit 2006
Ningde Amperex Technology Ltd.
IPR2023-00587, U.S. Patent No. 10,964,987
Page 11 of 14

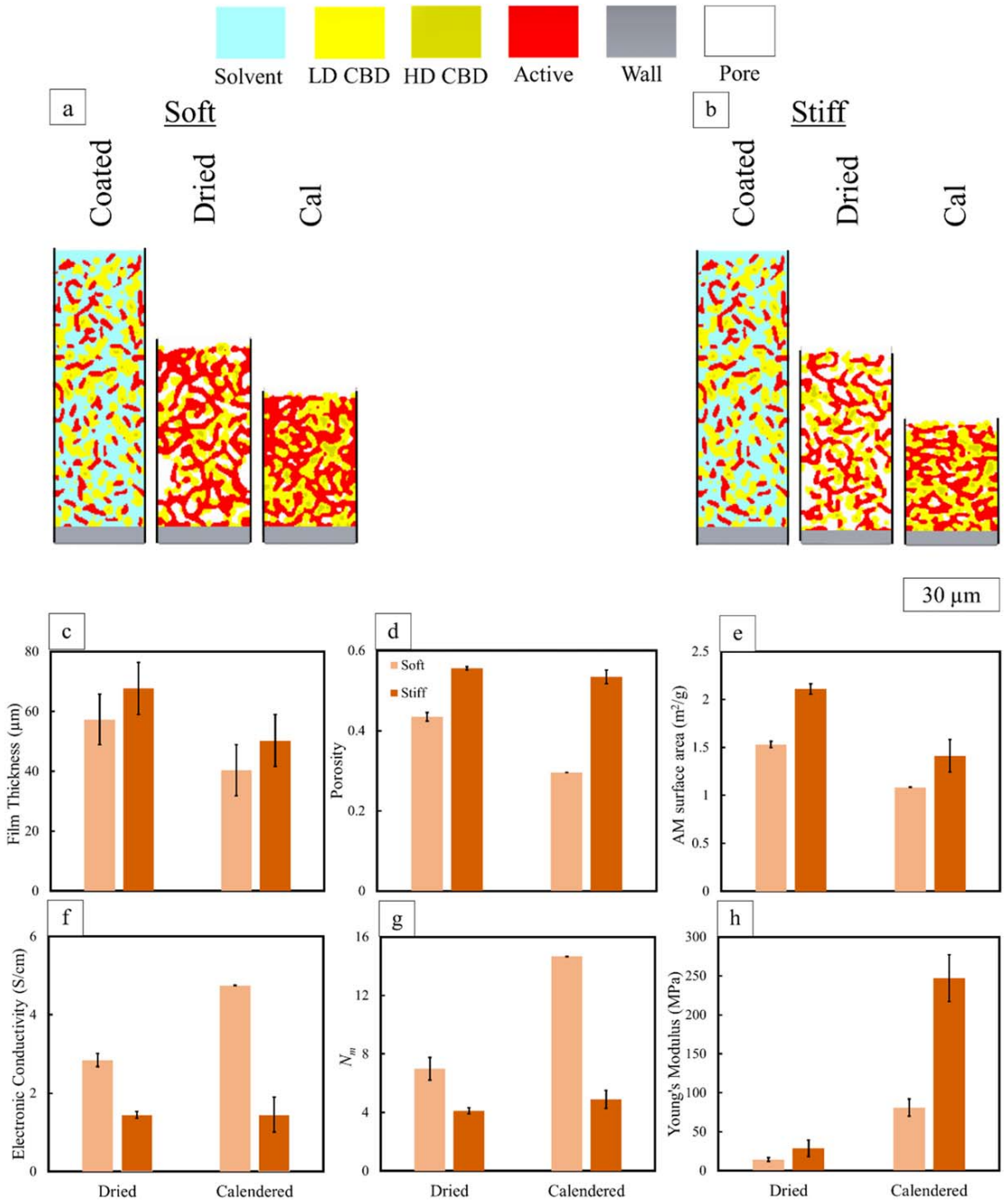


Figure 10. Simulated cross sections for (a) soft and (b) stiff AM. Remainder of properties (c)–(h) are the same as those in Fig. 5.

orientation differences start to diminish. Calendering clearly rotates disk-shaped particles to a more flat orientation, but this has little effect on the property trends already evident at the end of drying.

(6) The AM stiffness, when changed independently from other particle characteristics, had a significant effect on all the determined electrode properties. This suggests that this is a particle property worthy of further investigation.

These results can guide material selection and electrode design by improving our understanding of fundamental interactions at the particle level and their relationship to electrode properties of interest. For example, the MPSP model results suggest that small soft spherical particles favor electronic pathways. Whereas, the model results suggest using large stiff rods that are oriented vertically when the goal is to maximize ionic conductivity. The model also suggests that gradient-type electrodes could take advantage of the differences in electronic and ionic transport with changes to active material morphology.

Finally, it is worth mentioning that fabricating a perfectly homogenous microstructure is both challenging and expensive. It involves meticulous monitoring of the particle size, shape, orientation, and stiffness plus the subsequent microstructure properties during different manufacturing processes. The results of this work provide some information for designing new electrodes with purposeful through-plane heterogeneity. In future work we intend

Exhibit 2006
Ningde Amperex Technology Ltd.
IPR2023-00587, U.S. Patent No. 10,964,987

to use the MPSP model to assist in the design of multi-layered electrodes, i.e., having a gradient in porosity achieved using a dual slot die process.[69]

ORCID

M. Nikpour https://orcid.org/0000-0001-6069-0611

References

1. M. Nikpour, N. Barrett, Z. Hillman, A. I. Thompson, B. A. Mazzeo, and D. R. Wheeler, "A model for investigating sources of Li-ion battery electrode heterogeneity—part I: electrode drying and calendering processes." *Submitted to J. Electrochem. Soc.*, **168**, 060547 (2021).
2. Y. Yang, R. Xu, K. Zhang, S. J. Lee, L. Mu, P. Liu, C. K. Waters, S. Spence, Z. Xu, and C. Wei, "Quantification of heterogeneous degradation in Li-ion batteries." *Adv. Energy Mater.*, **9**, 1900674 (2019).
3. R. Xu, Y. Yang, F. Yin, P. Liu, P. Cloetens, Y. Liu, F. Lin, and K. Zhao, "Heterogeneous damage in li-ion batteries: experimental analysis and theoretical modeling." *J. Mech. Phys. Solids*, **129**, 160 (2019).
4. M. Mühlbauer, A. Schökel, M. Etter, V. Baran, and A. Senyshyn, "Probing chemical heterogeneity of Li-ion batteries by in operando high energy X-ray diffraction radiography." *J. Power Sources*, **403**, 49 (2018).
5. P. Liu, R. Xu, Y. Liu, F. Lin, and K. Zhao, "Computational modeling of heterogeneity of stress, charge, and cyclic damage in composite electrodes of Li-Ion batteries." *J. Electrochem. Soc.*, **167**, 040527 (2020).
6. J. R. Izzo, A. S. Joshi, K. N. Grew, W. K. Chiu, A. Tkachuk, S. H. Wang, and W. Yun, "Nondestructive reconstruction and analysis of SOFC anodes using X-ray computed tomography at sub-50 nm resolution." *J. Electrochem. Soc.*, **155**, B504 (2008).
7. J. Joos, T. Carraro, A. Weber, and E. Ivers-Tiffée, "Reconstruction of porous electrodes by FIB/SEM for detailed microstructure modeling." *J. Power Sources*, **196**, 7302 (2011).
8. Y.-C. K. Chen-Wiegart, Z. Liu, K. T. Faber, S. A. Barnett, and J. Wang, "3D analysis of a $LiCoO_2$–$Li(Ni_{1/3}Mn_{1/3}Co_{1/3})O_2$ Li-ion battery positive electrode using X-ray nano-tomography." *Electrochem. Commun.*, **28**, 127 (2013).
9. Y.-B. Yi, C.-W. Wang, and A. Sastry, "Compression of packed particulate systems: simulations and experiments in graphitic Li-ion anodes." *J. Eng. Mater. Technol.*, **128**, 73 (2006).
10. C.-W. Wang and A. M. Sastry, "Mesoscale modeling of a Li-ion polymer cell." *J. Electrochem. Soc.*, **154**, A1035 (2007).
11. N. Siddique and F. Liu, "Process based reconstruction and simulation of a three-dimensional fuel cell catalyst layer." *Electrochim. Acta*, **55**, 5357 (2010).
12. A. Awarke, M. Wittler, S. Pischinger, and J. Bockstette, "A 3D mesoscale model of the collector-electrode interface in Li-ion batteries." *J. Electrochem. Soc.*, **159**, A798 (2012).
13. Z. Liu, D. L. Wood, and P. P. Mukherjee, "Evaporation induced nanoparticle—binder interaction in electrode film formation." *Phys. Chem. Chem. Phys.*, **19**, 10051 (2017).
14. M. Stein, A. Mistry, and P. P. Mukherjee, "Mechanistic understanding of the role of evaporation in electrode processing." *J. Electrochem. Soc.*, **164**, A1616 (2017).
15. C. S. Giménez, B. Finke, C. Schilde, L. Froböse, and A. Kwade, "Numerical simulation of the behavior of lithium-ion battery electrodes during the calendaring process via the discrete element method." *Powder Technol.*, **349**, 1 (2019).
16. Z. Song, *Modeling and Simulation Of Heat of Mixing in Li-ion Batteries.*, Purdue University: Master's thesis (2015), 10.1016/j.powtec.2019.03.020.
17. N. Susarla, S. Ahmed, and D. W. Dees, "Modeling and analysis of solvent removal during Li-ion battery electrode drying." *J. Power Sources*, **378**, 660 (2018).
18. M. M. Forouzan, C.-W. Chao, D. Bustamante, B. A. Mazzeo, and D. R. Wheeler, "Experiment and simulation of the fabrication process of lithium-ion battery cathodes for determining microstructure and mechanical properties." *J. Power Sources*, **312**, 172 (2016).
19. S. A. Roberts, V. E. Brunini, K. N. Long, and A. M. Grillet, "A framework for three-dimensional mesoscale modeling of anisotropic swelling and mechanical deformation in lithium-ion electrodes." *J. Electrochem. Soc.*, **161**, F3052 (2014).
20. T. Hutzenlaub, S. Thiele, N. Paust, R. Spotnitz, R. Zengerle, and C. Walchshofer, "Three-dimensional electrochemical Li-ion battery modelling featuring a focused ion-beam/scanning electron microscopy based three-phase reconstruction of a LiCoO 2 cathode." *Electrochim. Acta*, **115**, 131 (2014).
21. B. T. Habte and F. Jiang, "Microstructure reconstruction and impedance spectroscopy study of $LiCoO_2$, $LiMn_2O_4$ and $LiFePO_4$ Li-ion battery cathodes." *Microporous Mesoporous Materials*, **268**, 69 (2018).
22. D. E. Stephenson, B. C. Walker, C. B. Skelton, E. P. Gorzkowski, D. J. Rowenhorst, and D. R. Wheeler, "Modeling 3D microstructure and ion transport in porous Li-ion battery electrodes." *J. Electrochem. Soc.*, **158**, A781 (2011).
23. M. Karplus, Development of multiscale models for complex chemical systems from H+H2 to biomolecules (Nobel lecture). Angewandte Chemie International Edition, 9992 (2014), 10.1002/anie.201403924.
24. W.-H. Ryu, S.-J. Lim, W.-K. Kim, and H. Kwon, "3-D dumbbell-like $LiNi_{1/3}Mn_{1/3}Co_{1/3}O_2$ cathode materials assembled with nano-building blocks for lithium-ion batteries." *J. Power Sources*, **257**, 186 (2014).
25. P. Subalakshmi and A. Sivashanmugam, "CuO nano hexagons, an efficient energy storage material for Li-ion battery application." *J. Alloys Compd.*, **690**, 523 (2017).
26. X. Gao, J. Bao, G. Pan, H. Zhu, P. Huang, F. Wu, and D. Song, "Preparation and electrochemical performance of polycrystalline and single crystalline CuO nanorods as anode materials for Li ion battery." *J. Phys. Chem. B*, **108**, 5547 (2004).
27. B. T. Habte and F. Jiang, "Effect of microstructure morphology on Li-ion battery graphite anode performance: Electrochemical impedance spectroscopy modeling and analysis." *Solid State Ionics*, **314**, 81 (2018).
28. V. A. Sethuraman, M. J. Chon, M. Shimshak, N. Van Winkle, and P. R. Guduru, "In situ measurement of biaxial modulus of Si anode for Li-ion batteries." *Electrochem. Commun.*, **12**, 1614 (2010).
29. K. Nelson, J. Harlow, and J. Dahn, "A comparison of NMC/graphite pouch cells and commercially available $LiCoO_2$/graphite pouch cells tested to high potential." *J. Electrochem. Soc.*, **165**, A456 (2018).
30. S. Goriparti, E. Miele, F. De Angelis, E. Di Fabrizio, R. P. Zaccaria, and C. Capiglia, "Review on recent progress of nanostructured anode materials for Li-ion batteries." *J. Power Sources*, **257**, 421 (2014).
31. M. D. Bhatt and J. Y. Lee, "High capacity conversion anodes in Li-ion batteries: A review." *Int. J. Hydrogen Energy*, **44**, 10852 (2019).
32. Y. H. Lee, J. Min, K. Lee, S. Kim, S. H. Park, and J. W. Choi, "Low molecular weight spandex as a promising polymeric binder for $LiFePO_4$ electrodes." *Adv. Energy Mater.*, **7**, 1602147 (2017).
33. Y.-H. Chen, C.-W. Wang, G. Liu, X.-Y. Song, V. Battaglia, and A. M. Sastry, "Selection of conductive additives in li-ion battery cathodes: A numerical study." *J. Electrochem. Soc.*, **154**, A978 (2007).
34. R. M. German and S. J. Park, *Handbook Of Mathematical Relations In Particulate Materials Processing: Ceramics, Powder Metals, Cermets, Carbides, Hard Materials, And Minerals.* (Wiley, New York, NY) 3 (2009).
35. D. T. Danielson, D. K. Sparacin, J. Michel, and L. C. Kimerling, "Surface-energy-driven dewetting theory of silicon-on-insulator agglomeration." *J. Appl. Phys.*, **100**, 083507 (2006).
36. G. Bluvol, M. Kässberger, and F. Reichhart, "Optimizing solids and rheology in blade coating using pigment blends-part." *O PAPEL*, **11**, 55 (2011).
37. M. Schmitt, P. Scharfer, and W. Schabel, "Slot die coating of lithium-ion battery electrodes: investigations on edge effect issues for stripe and pattern coatings." *J. Coat. Technol. Res.*, **11**, 57 (2014).
38. M. Schmitt, *Slot Die Coating Of Lithium-Ion Battery Electrodes.* (KIT Scientific Publishing)(Germany) (2016).
39. T.-T. Nguyen, A. Demortière, B. Fleutot, B. Delobel, C. Delacourt, and S. J. Cooper, "The electrode tortuosity factor: why the conventional tortuosity factor is not well suited for quantifying transport in porous Li-ion battery electrodes and what to use instead." *NPJ Comput. Mater.*, **6**, 1 (2020).
40. T. Satyavani, B. R. Kiran, V. R. Kumar, A. S. Kumar, and S. Naidu, "Effect of particle size on dc conductivity, activation energy and diffusion coefficient of lithium iron phosphate in Li-ion cells." *Engineering Science and Technology, an International Journal*, **19**, 40 (2016).
41. L. Pang, Y. Yang, L. Wu, F. Wang, and H. Meng, "Effect of particle sizes on the physical and mechanical properties of briquettes." *Energies*, **12**, 3618 (2019).
42. M. A. Stamps, J. W. Eischen, and H.-Y. Shadow Huang, "Particle-and crack-size dependency of lithium-ion battery materials $LiFePO_4$." *AIMS Mater. Sci*, **3**, 190 (2016).
43. D.-W. Chung, P. R. Shearing, N. P. Brandon, S. J. Harris, and R. E. Garcia, "Particle size polydispersity in Li-ion batteries." *J. Electrochem. Soc.*, **161**, A422 (2014).
44. J. Li, C. Daniel, and D. Wood, "Materials processing for lithium-ion batteries." *J. Power Sources*, **196**, 2452 (2011).
45. R. Vacassy, H. Hofmann, N. Papageorgiou, and M. Grätzel, "Influence of the particle size of electrode materials on intercalation rate and capacity of new electrodes." *J. Power Sources*, **81-82**, 621 (1999).
46. A. Sen Gupta, "Role of particle size, shape, and stiffness in design of intravascular drug delivery systems: insights from computations, experiments, and nature." . *Wiley Interdisciplinary Reviews: Nanomedicine and Nanobiotechnology*, **8**, 255 (2016).
47. S. B. Jones and S. P. Friedman, "Particle shape effects on the effective permittivity of anisotropic or isotropic media consisting of aligned or randomly oriented ellipsoidal particles." *Water Resour. Res.*, **36**, 2821 (2000).
48. A. Awarke, S. Lauer, S. Pischinger, and M. Wittler, "Percolation–tunneling modeling for the study of the electric conductivity in $LiFePO_4$ based Li-ion battery cathodes." *J. Power Sources*, **196**, 405 (2011).
49. C. W. Wang, K. A. Cook, and A. M. Sastry, "Conduction in multiphase particulate/fibrous networks: Simulations and experiments on Li-ion anodes." *J. Electrochem. Soc.*, **150**, A385 (2003).
50. X. Cheng, A. Sastry, and B. Layton, "Transport in stochastic fibrous networks." *J. Eng. Mater. Technol.*, **123**, 12 (2001).
51. M. Abe, A. Yamamoto, M. Orita, T. Ohkubo, H. Sakai, and N. Momozawa, "Control of particle alignment in water by an alternating electric field." *Langmuir*, **20**, 7021 (2004).
52. M. Ebner, D. W. Chung, R. E. Garcia, and V. Wood, "Tortuosity anisotropy in lithium-ion battery electrodes." *Adv. Energy Mater.*, **4**, 1301278 (2014).
53. A. Jean, F. Willot, S. Cantournet, S. Forest, and D. Jeulin, "Large-scale computations of effective elastic properties of rubber with carbon black fillers." *Int. J. Multiscale Comput. Eng.*, **9**, 271 (2011).
54. A. C. Ngandjong, T. Lombardo, E. N. Primo, M. Chouchane, A. Shodiev, O. Arcelus, and A. A. Franco, "Investigating electrode calendering and its impact on electrochemical performance by means of a new discrete element method model: Towards a digital twin of Li-Ion battery manufacturing." *J. Power Sources*, **485**, 229320 (2021).
55. E. J. Cheng, N. J. Taylor, J. Wolfenstine, and J. Sakamoto, "Elastic properties of lithium cobalt oxide ($LiCoO_2$)." *Journal of Asian Ceramic Societies*, **5**, 113 (2017).
56. Carbon, (2021), Carbon - Graphite Materials (https://azom.com/properties.aspx?ArticleID=516).

Exhibit 2006
Ningde Amperex Technology Ltd.
IPR2023-00587, U.S. Patent No. 10,964,987

57. Sandia 2018 Large-scale Atomic/Molecular Massively Parallel Simulator (https://lammps.sandia.gov/cite.html).Version 12 Dec.
58. M. Nikpour, "MPSP model." *Nikpour M. 2021 MPSP model (Accessed on May 4)*, **1**, 1 (2021), (https://github.com/mnikpour/USER-MPSP.git).
59. K. Rollag, D. Juarez-Robles, Z. Du, D. L. Wood III, and P. P. Mukherjee, "Drying temperature and capillarity-driven crack formation in aqueous processing of li-ion battery electrodes." *ACS Appl. Energy Mater.*, **2**, 4464 (2019).
60. C. R. Hernandez, A. Etiemble, T. Douillard, D. Mazouzi, Z. Karkar, E. Maire, D. Guyomard, B. Lestriez, and L. Roué, "A Facile and very effective method to enhance the mechanical strength and the cyclability of Si-based electrodes for Li-ion batteries." *Adv. Energy Mater.*, **8**, 1701787 (2018).
61. T. Jia, Y. Zhang, and J. Chen, "Simulation of granular packing of particles with different size distributions." *Comput. Mater. Sci.*, **51**, 172 (2012).
62. A. P. Philipse, "The random contact equation and its implications for (colloidal) rods in packings, suspensions, and anisotropic powders." *Langmuir*, **12**, 1127 (1996).
63. J. O. Freeman, S. Peterson, C. Cao, Y. Wang, S. V. Franklin, and E. R. Weeks, "Random packing of rods in small containers." *Granular Matter*, **21**, 1 (2019).
64. B. D. Lubachevsky, F. H. Stillinger, and E. N. Pinson, "Disks vs spheres: Contrasting properties of random packings." *J. Stat. Phys.*, **64**, 501 (1991).
65. G. Cho, J. Dodds, and J. C. Santamarina, "Particle shape effects on packing density, stiffness, and strength: natural and crushed sands." *J. Geotech. Geoenviron. Eng.*, **133**, 1474 (2007).
66. H. Dreger, W. Haselrieder, and A. Kwade, "Influence of dispersing by extrusion and calendering on the performance of lithium-ion battery electrodes." *Journal of Energy Storage*, **21**, 231 (2019).
67. W. D. Callister and D. G. Rethwisch, *Materials Science and Engineering: An Introduction.* (Wiley, New York, NY) 9th ed. (2014).
68. M. Tunák and A. Linka, "Analysis of planar anisotropy of fibre systems by using 2D Fourier transform." *Fibres Textiles East. Eur.*, **15**, 86 (2007).
69. Y. Dai and V. Srinivasan, "On graded electrode porosity as a design tool for improving the energy density of batteries." *J. Electrochem. Soc.*, **163**, A406 (2015).